Magnetic 2D $RuCl_3$

April 26, 2023 · salve-project.de/newspress/magnetic_2DRuCl3.html

April 26, 2023 – Layered ruthenium chloride (α-$RuCl_3$) is one of the few materials in which an exotic magnetic state, the quantum spin liquid, might be realized, yet almost everything known about it comes from bulk crystals. A team from the Universities of Heidelberg, Kassel and Ulm, the Max Planck Institute for Solid State Research in Stuttgart and the Bundeswehr University Munich, together with colleagues at Trinity College Dublin, has now exfoliated α-$RuCl_3$ in liquid without additives, sorted the nanosheets by size, confirmed their structural integrity with aberration-corrected low-voltage TEM, and followed how magnetism, optical response and stability change with nanosheet size.

Why does a brittle, dark chloride attract physicists who dream of quantum computers? Layered α-$RuCl_3$ is a candidate for quantum spin liquid states, because its magnetic Ru^{3+} ions sit on a honeycomb lattice with strong relativistic spin–orbit coupling. In the spin-1/2 model with bond-dependent interactions, the Kitaev model, the ground state is a quantum spin liquid (QSL), a topological state that holds the promise of coherent transport of quantum information and of fractional excitations[1], exotic phenomena in which an electron splits into well-defined quasiparticles. On the Kitaev honeycomb lattice[2] these take the form of gauge fluxes and Majorana fermions[3]. So far such fractional excitations exist only in theory; realizing them experimentally in α-$RuCl_3$ or any other material would count as a breakthrough for quantum computation[4].

Real crystals are less tidy than the model. Non-Kitaev interactions in $RuCl_3$ lead to long-range antiferromagnetic order at low temperatures[5]. In single crystals, this order sets in either in one sharp phase transition at a Néel temperature of T_N = 7 K, as seen in magnetic susceptibility and specific heat[5], or in a sequence of two transitions at T_{N1} ≈ 14 K and T_{N2} ≈ 8 K[6–9]. The number, position and shape of these transitions are thought to depend on the stacking order and stacking faults of the hexagonal Ru^{3+} layers. In polycrystalline samples, single antiferromagnetic transitions have been reported at T_N = 11 K[10], 13 K[11] and 15.6 K[12].

Almost all of this work concerns the bulk. What happens after exfoliation is far less clear, although it matters: delaminating the crystal reduces the stacking disorder that is held responsible for the pronounced antiferromagnetic order[5],[9]. α-$RuCl_3$ has recently been exfoliated chemically[9] and electrochemically[13], but in both cases the material lost its original electronic and magnetic properties because it was electron-doped. An alternative is liquid phase exfoliation (LPE), in which the layers are peeled apart mechanically by the forces that collapsing cavitation bubbles exert on the crystal[14] and the sheets are stabilized colloidally by suitable surfactants or solvents[15]. The method has been applied to well over fifteen classes of layered materials, among them transition metal dichalcogenides (TMDs)[19], transition metal hexathiohypodiphosphates ($M_2P_2S_6$)[21],[22], III–VI and IV–VI semiconductors[23], pnictogens[24], silicates[25], oxides[26], hydroxides[27] and other minerals[28], as well as synthetic crystals such as organic polymers[29] and covalent organic 2D frameworks[30]. Usually neither a phase transition nor heavy doping occurs, which makes LPE a promising route to the layer-number-dependent properties of α-$RuCl_3$.

The team led by Claudia Backes, with the Ulm electron microscopy group of Ute Kaiser, therefore exfoliated α-$RuCl_3$ without any additive by sonication-assisted LPE under inert conditions. To separate the effect of nanosheet size and thickness on the optical and magnetic response, the dispersion was sorted into fractions by established centrifugation techniques[31], and the lateral size and thickness distributions were quantified by statistical atomic force microscopy (AFM) (Fig. 1). The structural integrity of the nanosheets was checked by a combination of transmission electron microscopy (TEM), Raman spectroscopy, X-ray diffraction (XRD) and X-ray photoelectron spectroscopy (XPS). The magnetic susceptibility was measured for three fractions of different nanosheet size, both in dispersion and on drop-cast films. Extinction and absorbance spectroscopy on the dispersions yielded metrics for the concentration and the average layer number. Finally, time- and temperature-dependent absorbance measurements quantified how stable the nanosheets are in air. How the material was exfoliated and sorted is described in the first box.

α-$RuCl_3$: exfoliation and cascade centrifugation

The starting material, α-$RuCl_3$ single crystals grown by chemical vapour transport, forms crystallites up to about 1 mm in size; Raman spectroscopy and powder XRD confirmed its crystallinity. Ground crystals were exfoliated by bath sonication under inert gas in dried, distilled and degassed N-cyclohexyl-2-pyrrolidone (CHP). Pyrrolidone-based solvents are known to stabilize the LPE products of many layered crystals and, in addition, to passivate the sheet surface and suppress decomposition[21], an effect attributed to strong solvent–surface interactions and a protective solvation shell.

The resulting stock dispersion, a polydisperse mixture of nanosheets of all sizes and thicknesses, was sorted by liquid cascade centrifugation (LCC)[31]. The first step at a low relative centrifugal force (RCF) of 100 g sedimented the large, thick and unexfoliated sheets. The supernatant was centrifuged again at 400 g, the sediment redispersed in a small volume of fresh solvent as a concentrated sample, and the supernatant passed on to the next step, at 1k g, 3k g, 6k g, 12k g, 22k g and finally 50k g (the unit g stands for multiples of the earth's gravitational acceleration). The

first sediment and the last supernatant were discarded, since they contain mostly unexfoliated and defective material, respectively. Seven fractions remained, each labelled by the lower and upper RCF between which its sheets were trapped: the sediment collected at 6k g from the supernatant of the 3k g step is the 3–6k g fraction. The fractions 0.1–0.4k g, 6–12k g and 22–50k g served throughout the study as representatives of large, medium and small nanosheets.

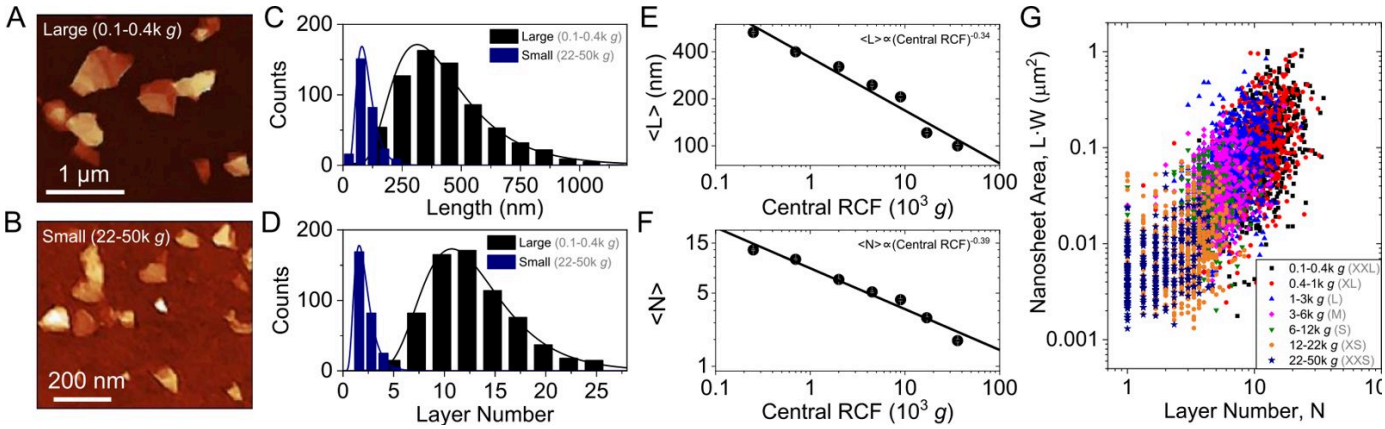

Fig. 1: AFM images of large and small nanosheet fractions (A, B), size and layer-number histograms (C, D), power-law dependence of mean length and layer number on centrifugal force (E, F), area versus layer number (G).

The sorting worked as intended, and statistical AFM on more than a hundred sheets per fraction put numbers to it: both the mean length and the mean layer number fall with increasing centrifugal acceleration as power laws, and thinner sheets tend to be smaller, as is typical for LPE[38] (Fig. 1). The details of the measurement, including the conversion of AFM height into layer number, are collected in the second box.

α-$RuCl_3$: AFM statistics and layer number

For the AFM statistics the concentrated fractions were diluted with isopropanol and drop-cast on Si/SiO_2 wafer pieces. Line profiles were drawn across every sheet: the length is the longest dimension, the width the dimension perpendicular to it, and the height the average from both profiles (see[19],[32] for details). Representative images of the largest (0.1–0.4k g) and the smallest (22–50k g) fraction are shown in Figs. 1A and 1B, their lateral size and layer-number distributions in Figs. 1C and 1D. Both are lognormal and shift to markedly smaller values for the fraction isolated at higher speed.

The apparent AFM height of liquid-exfoliated nanosheets is typically overestimated, because impurities, solvent residues, the chemical potential and the measurement parameters add to it, but it stays proportional to the crystallographic thickness[21],[33]–[35]. The problem is solved by a step-height analysis on incompletely exfoliated sheets[21],[33],[36]: line profiles across terraces on more than 100 structures, plotted in ascending order, revealed regular steps in multiples of 1.5 nm, so the apparent height was divided by 1.5 nm to obtain the layer number.

Plotted against the central RCF of each fraction on a double-logarithmic scale (Figs. 1E and 1F), the arithmetic means follow power laws, $\langle N\rangle \propto RCF^{-0.34}$ and $\langle L\rangle \propto RCF^{-0.39}$. Similar behaviour is known from other 2D materials, although an exponent of −0.5 is usually expected for <L>, since the cut size scales with the inverse rotation rate[31]. The scatter plot of nanosheet area against layer number for all fractions (Fig. 1G) shows the decreasing average size with increasing centrifugation speed, some overlap between neighbouring fractions, and the correlation that thin sheets are small and thick sheets are large, a consequence of delamination and tearing occurring side by side[38].

Are the sheets still α-$RuCl_3$ after sonication and centrifugation? To answer this, the structural integrity and crystallinity were examined by TEM, Raman spectroscopy, XPS and XRD; the results are summarized in Fig. 2. For TEM, a dispersion from which only the unexfoliated material had been removed at 100 g was drop-cast on Quantifoil grids in a nitrogen atmosphere, a choice that kept exposure to air to a minimum, since the centrifugation had to be done in sealed vials outside the glovebox. CHP residues were removed in the pre-vacuum of the microscope (about 2×10^{-5} mbar) at 150 °C for 40 min before low-dose high-resolution TEM (HRTEM) at 80 kV. The overview image in Fig. 2A shows a nanosheet several micrometres long with sharp edges, in line with the morphology seen in AFM. Selected area electron diffraction (SAED) from the region marked by the dashed circle gives sharp, bright spots, which confirm the crystallinity of the exfoliated material. The HRTEM images in Figs. 2B and 2C resolve the atomic lattice, and the fast Fourier transform in the inset of Fig. 2B underlines the crystalline character. The images agree well with a simulated trigonal lattice and with the literature[39].

The direct comparison with image simulations was the Ulm contribution, and it also showed what the electron beam does to the sheets (Fig. 3). An earlier study of exfoliated α-$RuCl_3$[39] had shown that the two commonly observed phases, trigonal (space group $P3_112$[11]) and monoclinic (C2/m[37]), can be told apart in high-resolution STEM images along the c* direction of the crystal by their different stacking order. The researchers therefore simulated HRTEM images of six-layer stacks of trigonal α-$RuCl_3$ (Fig. 3F), of the monoclinic polymorph (Fig. 3G) and, for complete-

ness, of β-$RuCl_3$ (space group $P6_3/mcm$[16], Fig. 3H) along c*, using a multislice code[40]. The simulation parameters matched the aberration state of the microscope measured before the experiment (C_3 ≈ –7.5 mm, C_5 ≈ 2.7 mm), which gives bright atom contrast at the chosen defocus of about –4 nm[17]. The experimental image (Fig. 3E) agrees best with the trigonal structure, judged by the different contrast of the atomic columns. It also shows vacancies and stacking defects, recognizable as weaker atomic columns and distorted lattice regions, which are mainly caused by the electron irradiation during image acquisition. Small and thin nanosheets were so beam-sensitive even at 80 kV that their lattice changed substantially under illumination; ultrathin sheets, below about six layers as estimated with the EELS log-ratio method[18], could not be imaged at atomic resolution at all.

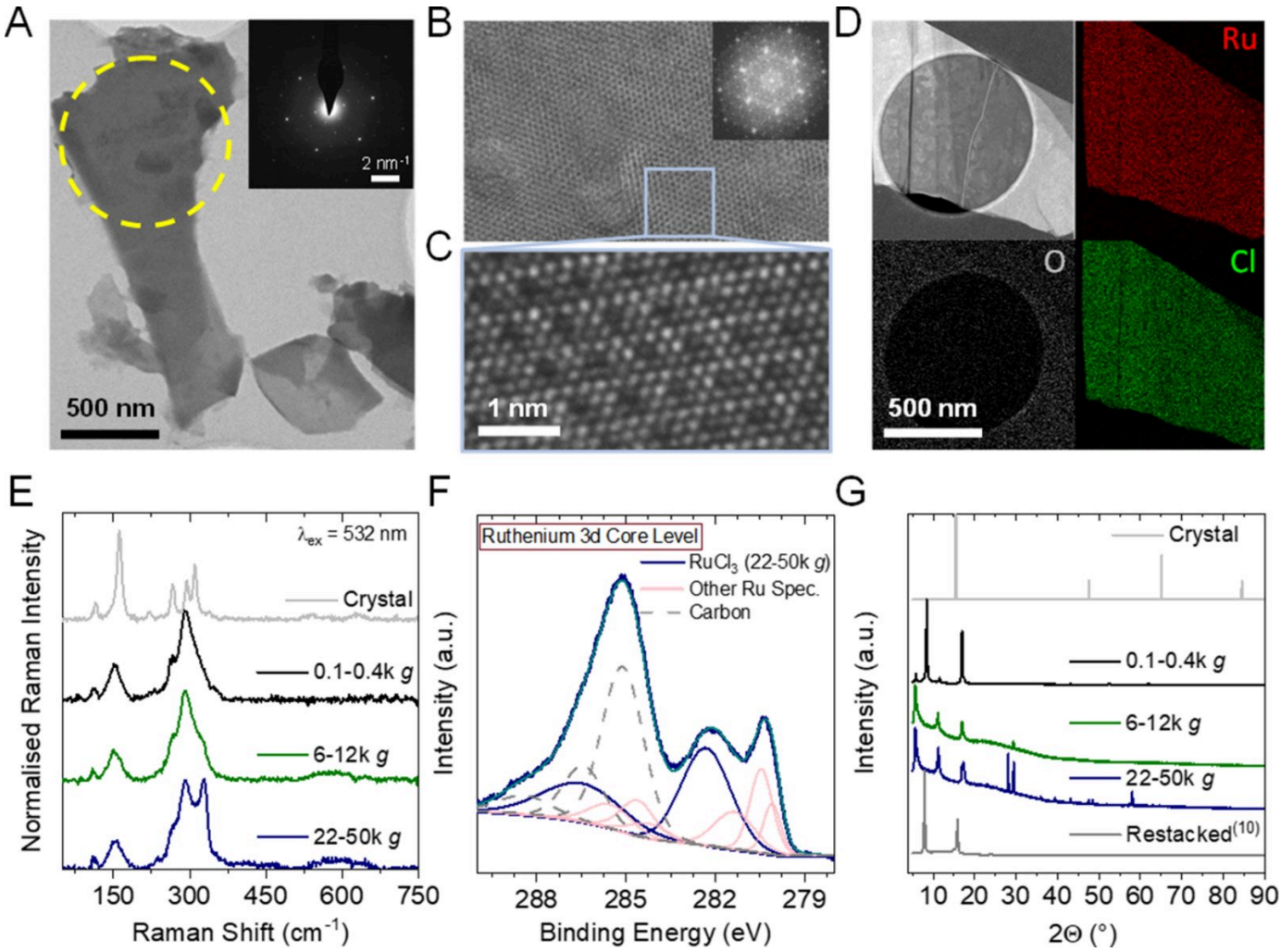

Fig. 2: TEM overview with SAED (A), HRTEM of the atomic lattice (B, C), HAADF-STEM with EDX maps of Ru, Cl and O (D), Raman spectra (E), Ru 3d XPS (F) and powder XRD (G) of size-selected fractions compared with the bulk.

The chemistry was checked in the same microscope. Energy-dispersive X-ray (EDX) mapping in scanning TEM (STEM) on free-standing sheets gave the high-angle annular dark-field image and the elemental maps of ruthenium (red), chlorine (green) and oxygen (white) shown in Fig. 2D. They confirm the stoichiometry and suggest only minute oxidation, a finding backed by core-loss electron energy loss spectroscopy, in which the Cl L and K edges and the Ru M series were resolved while oxygen was barely detectable. For the probed areas the composition came out as $RuCl_{2.6}O_{0.02}$, $RuCl_{2.7}O_{0.3}$ and $RuCl_{3.1}O_{0.01}$.

Individual sheets in the TEM are only part of the picture, and the smallest and thinnest ones cannot be probed there reliably. The team therefore turned to ensemble measurements on drop-cast films: Raman spectroscopy and XPS on gold-coated aluminium supports (Figs. 2E and 2F) and powder XRD on quartz (Fig. 2G), all prepared in an inert atmosphere. Together these methods told a more cautious story than the TEM: Raman showed no sign of decomposition, XPS found only about half of the surface still to be $RuCl_3$, and XRD revealed extra reflections that could be either decomposition products or an orientation effect. The findings are laid out in the third box.

α-$RuCl_3$: Raman, XPS and XRD on nanosheet ensembles

Raman spectra of the large, medium and small fractions (0.1–0.4k g, 6–12k g, 22–50k g) are shown in Fig. 2E together with an average spectrum of a single crystal. All modes of the bulk also appear in the exfoliated material, but considerably broadened, which is attributed to finite-size effects and the random orientation of the drop-cast sheets; a similar broadening has been seen in micromechanically cleaved nanosheets[20]. Since no new modes appear,

Raman gives no clear indication of decomposition after LPE and LCC. The decomposition products, however, may simply not be Raman-active or resonant with the excitation wavelength.

Hence XPS was measured as well. The ruthenium 3d core level spectrum of the fraction with the smallest sheets (22–50k g, Fig. 2F) contains, besides the expected $RuCl_3$ signal, contributions from carbon, elemental ruthenium, ruthenium oxide, hydroxide and oxyhydroxide (RuO_2, $Ru(OH)_3$ and $RuO(OH)_2$). Fitting the components indicates that only about 50 % of the sample surface was still $RuCl_3$ at the time of the measurement, with roughly 10 % of the signal from elemental ruthenium, 21 % from RuO_2 and 16 % from $Ru(OH)_3$.

The powder diffractograms of the large, medium and small fractions (Fig. 2G) differ from that of bulk α-$RuCl_3$, shown in grey. Compared with the recently reported pattern of randomly restacked $RuCl_3$ nanosheets[9], the most intense Bragg reflections of the exfoliated material appear at similar angles, and they are broadened, which points to structural distortion of the restacked material after drop-casting, in line with the Raman spectra. As the sheet size decreases, more reflections appear that cannot be assigned. They could stem from crystalline degradation products, which would show more clearly in samples with a higher surface-to-volume ratio. Alternatively, they could be an effect of preferential orientation: in large platelets the reflection geometry picks out mainly (001)-type reflections, while in smaller platelets, which lie less flat, out-of-plane reflections gain weight. In that case the additional reflections at higher angles 2Θ would belong to other polymorphs or decomposition products of $RuCl_3$. Simulations for different lattices and stacking orientations would be needed to decide, in particular because the reflections cannot be assigned to the species seen in XPS[9],[41].

Taken together, the ensemble measurements show that exfoliated α-$RuCl_3$ is prone to degradation. Since the material was exposed to air in most of these measurements, the degree of oxidation of the pristine sheets cannot be pinned down, but the TEM results, obtained with exposure to oxygen and water kept to a minimum, show very little oxidation of the material as made. The smallest and thinnest sheets are very sensitive to radiation damage in TEM and XPS alike, so their composition could not be determined directly; the absorbance spectra, however, have the same spectral profile for all fractions, which indicates the same initial composition even for the smallest sheets. The authors stressed that liquid-exfoliated nanosheets must be handled with special care, because their reactivity is much higher than that of the solid.

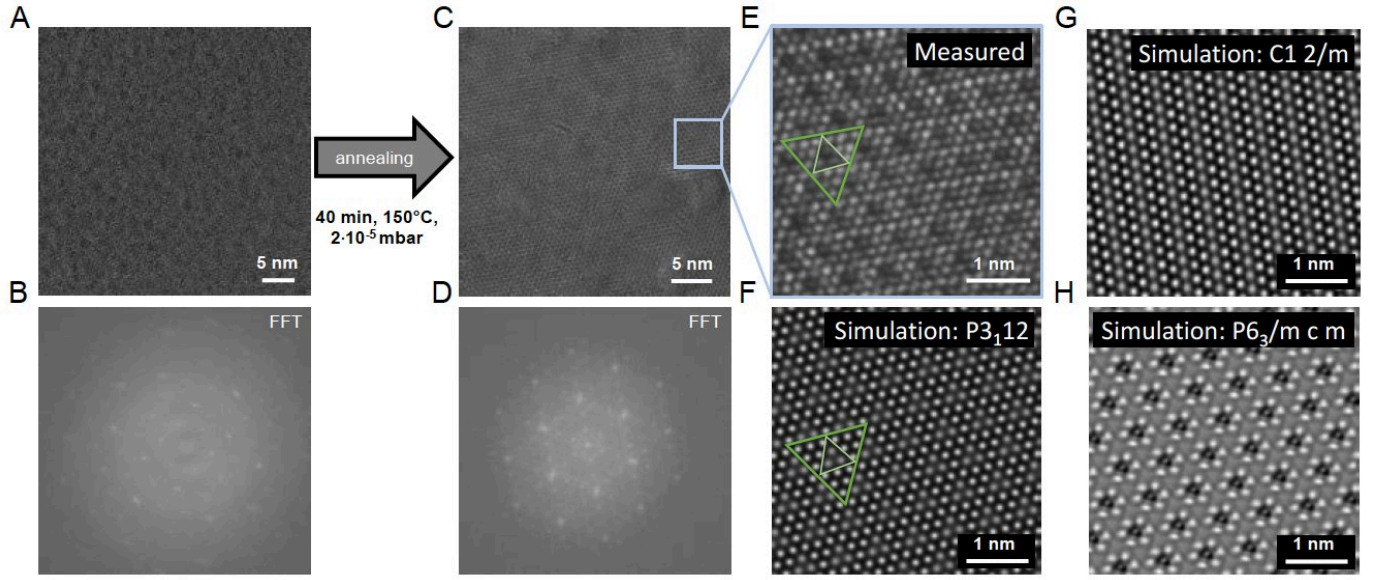

Fig. 3: HRTEM and FFT of a nanosheet before (A, B) and after (C, D) annealing in the microscope pre-vacuum, atomic-resolution detail (E), and multislice simulations of the trigonal (F), monoclinic (G) and β-$RuCl_3$ (H) lattices.

With the structure confirmed, the team turned to the question that motivates all interest in α-$RuCl_3$: its magnetism. The material is considered a possible realization of a two-dimensional QSL in its ground state[9],[42],[43]. Most studies so far have used micromechanically exfoliated (ME) nanosheets[20],[39],[44], a few have used liquid exfoliation[9], and none had looked at pristine, undoped nanosheets made by sonication-assisted LPE. Magnetic susceptibility was now measured in a superconducting quantum interference device (SQUID) magnetometer for the large, medium and small fractions, both dispersed in CHP and as drop-cast pellets deposited in an inert atmosphere (Fig. 4). The upshot: no quantum spin liquid, but a clear size effect. The broad antiferromagnetic anomaly of the bulk near 10 K disappears in the nanosheets, while a sharp transition appears at 2–3 K, and it becomes more pronounced the smaller the sheets. The numbers are given in the fourth box.

α-$RuCl_3$: susceptibility of dispersed and drop-cast nanosheets

Fig. 4A shows the low-temperature magnetic response of CHP-dispersed nanosheets of the three sizes, for two separately exfoliated batches each, together with the starting material. Because the solvent contributes a non-negligible background, the data were scaled to the susceptibility of the crystal at 50 K. The bulk crystal

shows a uniform Curie–Weiss-like rise of the magnetization on cooling from room temperature, followed by a broad anomaly at about 10 K that signals long-range antiferromagnetic order. In the dispersion of large sheets (0.1–0.4k g) this anomaly is suppressed; instead a sharp transition appears at T = 2 K (Fig. 4A, inset). The small sheets (22–50k g) show no transition in the accessible temperature range, while one of the two batches of medium-sized sheets (6–12k g) does. The low-temperature response of the small and medium dispersions differs between batches, which the researchers attributed to a combination of material decomposition, solvent effects and partial aggregation of the sheets on cooling.

For the drop-cast pellets (Fig. 4B) the high-temperature susceptibility runs proportional to the bulk. Below 75 K the platelets fall away from the bulk curve, which indicates stronger short-range antiferromagnetic correlations in the bulk than in the platelets. Medium and large sheets behave alike, with a broad, plateau-like hump at about 4 K and a sharp drop at the lowest temperatures (Fig. 4B, inset 1). In a low field of B = 0.01 T the hump turns into a well-resolved peak (inset 2), which marks long-range antiferromagnetic order at T_N = 3 K for the medium and large sheets; at B = 1 T this order is either suppressed or shifted below the accessible range. Reducing the size stabilizes the antiferromagnetic phase: the smallest sheets show a sharp susceptibility peak at 2.2 K even at B = 1 T (inset 1), although, for lack of material, the measurement at 0.01 T did not succeed for this fraction. At the same time the broad hump is absent for the smallest sheets, so their short-range antiferromagnetic correlations in this temperature range are weaker.

The overall tendency is that high-temperature antiferromagnetic correlations are suppressed on size reduction, while a sharp, rather 3D-like antiferromagnetic phase transition is stabilized. The authors argued that the low-temperature antiferromagnetic phase of the solid nanosheet samples is probably of the same nature as the phase marked by the sharp drop in susceptibility of the dispersed samples.

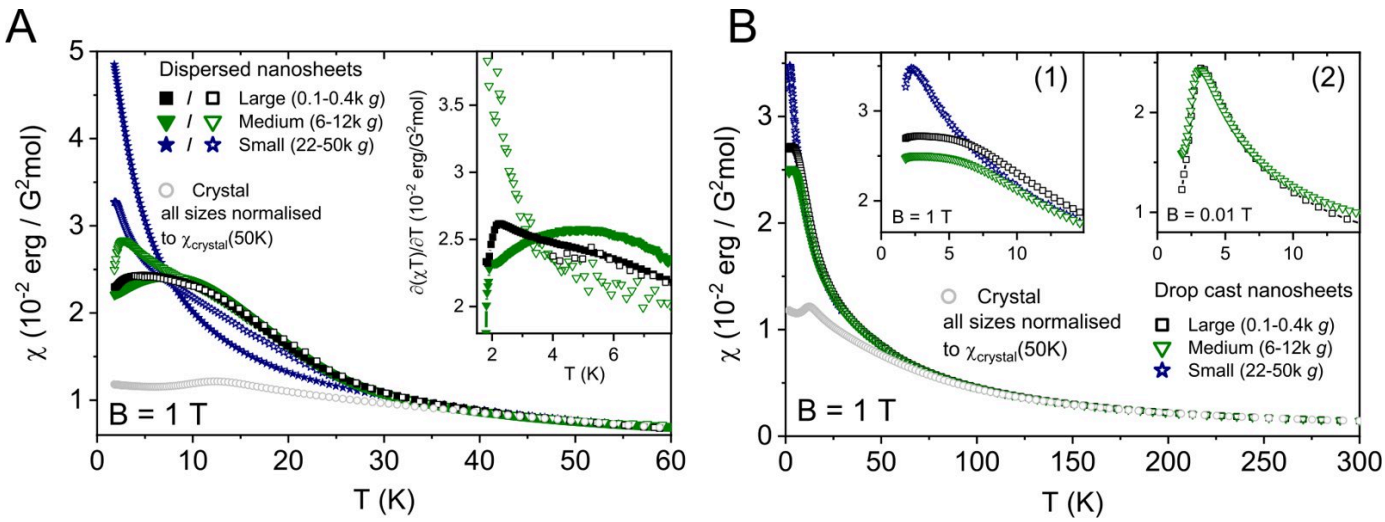

Fig. 4: Normalized magnetic susceptibility versus temperature of nanosheets dispersed in CHP (A) and of drop-cast nanosheets (B) for three sizes, compared with a bulk crystal; insets show the low-temperature transitions at 1 T and 0.01 T.

Size also leaves its mark in the optical spectra, though a surprisingly faint one. The size-selected fractions were measured by extinction and absorbance spectroscopy in transmission, where the extinction is the sum of absorption and scattering; to separate the two, the dispersions were additionally placed in the centre of an integrating sphere, which collects the scattered light, and the concentration of each fraction was determined by gravimetric weighing. As expected, large sheets scatter more than small ones (Figs. 5A and 5B), but compared with other LPE nanosheets such as TMDs, $Ni_2P_2S_6$ or layered hydroxides[21],[22],[27], the scattering contribution is much smaller. All fractions show two broad features at about 370 and 550 nm, and the extinction coefficient at 400, 500 and 600 nm hardly varies with sheet size (Fig. 5D, inset). This is unusual, because size-dependent scattering, edge and confinement effects and dielectric screening normally change the spectra of nanosheets in characteristic ways[21],[33], but it has a practical benefit: size-independent coefficients allow the concentration of α-$RuCl_3$ dispersions to be determined reliably by the Beer–Lambert law. The subtler systematic shifts, from which the team derived metrics for the layer number, are in the fifth box.

α-$RuCl_3$: spectroscopic metrics for layer number and size

Because the masses from gravimetry carry an uncertainty that propagates into the coefficient spectra, size-dependent trends were also studied on normalized spectra. These vary only slightly across the fractions, but exposure to air, especially at elevated temperature, changes the spectral profile markedly, so the samples start out with the same composition and their degradation can be followed by absorbance (see below). Intensity ratios in extinction or absorbance spectra usually scale with the lateral size, because edges and basal planes contribute differently to the electronic structure. The peak intensity ratio 370 nm/555 nm was therefore plotted against the mean lateral size from AFM and fitted with a previously reported model[45]. The fits are reasonable, but the change in the ratio is too small for a reliable size determination from UV–Vis spectroscopy alone.

The positions of the optical transitions shift systematically as well. Such shifts are often attributed to confinement and dielectric screening of excitons and typically scale with the layer number[21,33]. The centre-of-mass position of the peak at 375 nm, determined from the second derivative of the spectra (Fig. 5E), red-shifts with increasing nanosheet dimensions in both the extinction and the absorbance spectra and follows an empirical scaling with the mean layer number from AFM (Fig. 5F), in agreement with previous reports. This allows electronic transitions to be compared across material systems and gives a layer-number metric from either spectrum. The fit parameters are listed in Table 1 of the paper: for extinction, A_1 = –0.0019 nm^{-1}, B_1 = 1.68, A_2 = –0.0010 nm^{-1}, B_2 = 1, E_A^{ML} = 3.307 eV, E_A^{Bulk} = 3.224 eV and N_0 = 5.58; for absorbance, A_1 = –0.0018 nm^{-1}, B_1 = 1.75, A_2 = –0.0009 nm^{-1}, B_2 = 1, E_A^{ML} = 3.304 eV, E_A^{Bulk} = 3.253 eV and N_0 = 6.92. The resonances from the extinction spectra are increasingly red-shifted for thicker sheets compared with those from absorption, which is attributed to the growing contribution of light scattering from larger sheets, itself red-shifted relative to the absorbance (Fig. 5A).

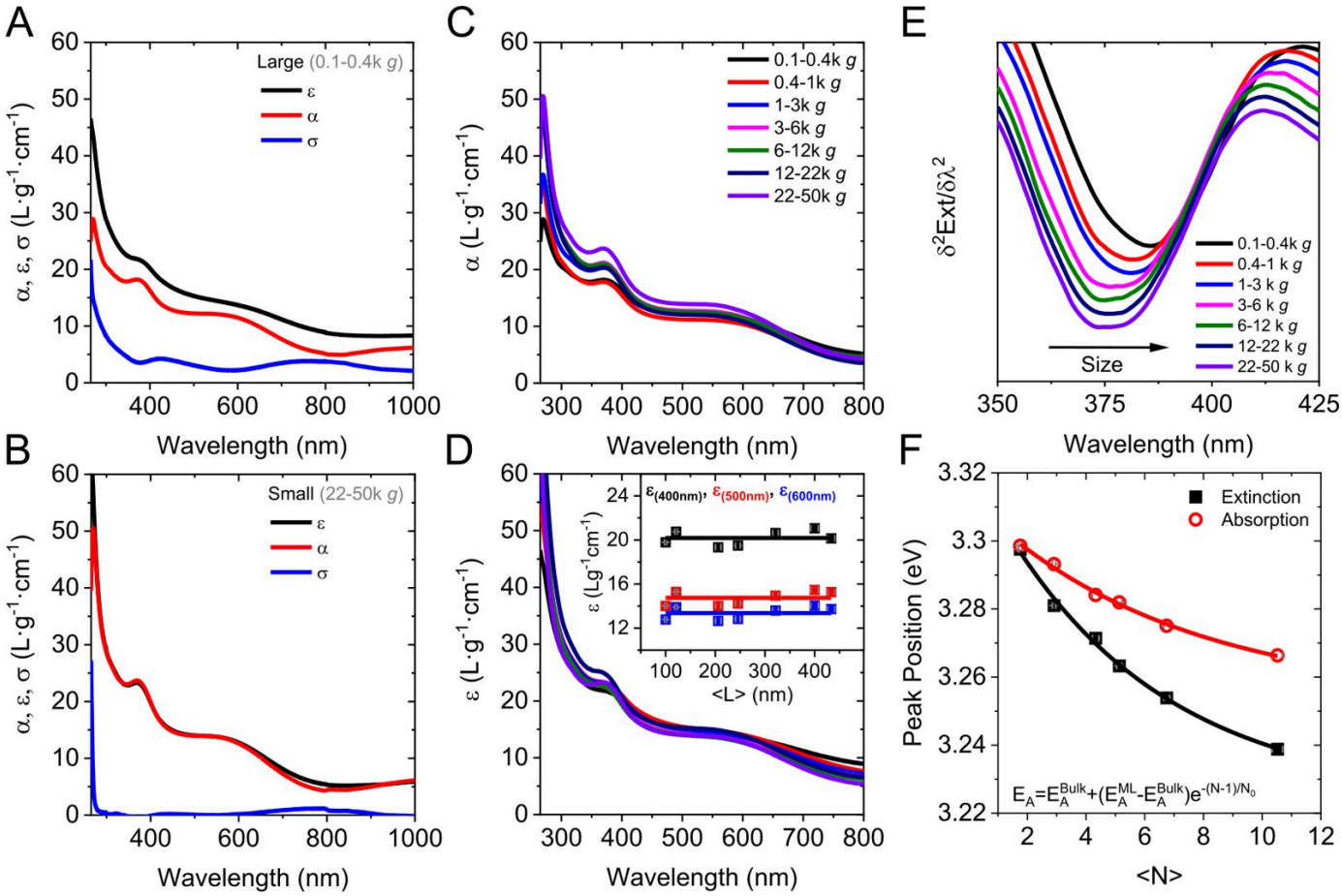

Fig. 5: Extinction, absorption and scattering spectra of large and small nanosheets (A, B), coefficient spectra of all fractions (C, D), second-derivative peak positions (E) and their scaling with layer number (F).

Nanosheets are often more sensitive to their environment than the bulk because of their much larger surface area, and several of the techniques above had hinted at oxidation. The team therefore quantified the degradation: dispersions of large, medium and small sheets were exposed to air and stirred at 20, 40 and 60 °C, with absorbance spectra taken at set intervals for up to 672 h, or 28 days (Fig. 6). The result is reassuring in one respect and cautionary in another: the half-lives are long, more than 30 days for every fraction even at 60 °C, but the activation energies are remarkably low, 6–19 kJ/mol, and they fall with decreasing sheet size, which points to degradation starting at the edges. The kinetic analysis is given in the sixth box.

α-$RuCl_3$: decomposition kinetics in air

Before each measurement the samples were bath-sonicated for about 2 min to rule out aggregation or sedimentation. The spectra of large sheets stirred at 60 °C (Fig. 6A) change substantially in the UV region over time, a sign of structural change, while in the visible region between 500 and 800 nm the signal decreases systematically with its shape retained, so that only $RuCl_3$ contributes there. The absorbance at 525 nm proved the best-behaved measure for all sizes and temperatures and follows a single exponential decay. Its natural logarithm plotted against stirring time gives straight lines (Fig. 6B), consistent with (pseudo) first-order kinetics. The authors cautioned that this simplicity is surprising: in solution a solvation cage can make the rate diffusion-controlled, edges and basal planes are different reaction sites, and XPS had found several products (oxides and hydroxides). The macroscopic average nevertheless follows (pseudo) first-order kinetics well, so lin-

ear fits on the semi-logarithmic scale, which have fewer degrees of freedom than exponential fits, were used to extract the half-lives.

Table 2 of the paper lists the result. For large sheets (0.1–0.4k g) the half-life is 2596 ± 46 h at 20 °C, 2212 ± 25 h at 40 °C and 1898 ± 49 h at 60 °C; for medium sheets (6–12k g) 2083 ± 24 h, 1440 ± 22 h and 974 ± 20 h; for small sheets (22–50k g) 1953 ± 84 h, 1237 ± 14 h and 769 ± 20 h. An Arrhenius plot of the logarithm of the half-life against the inverse temperature (Fig. 6C) is reasonably linear even with only three temperatures per size and gives activation energies of 18.9 ± 0.8 kJ/mol for the large, 15.4 ± 0.8 kJ/mol for the medium and 6.4 ± 0.2 kJ/mol for the small sheets. Plotted against the mean sheet length (Fig. 6D), the activation energy rises with size, which implies that decomposition needs less energy at the edges than on the basal planes. The values are lower than for WS_2 monolayers in aqueous surfactant or for $Ni_2P_2S_6$[21], but the half-lives are relatively long: although degradation sets in at moderate temperatures, the time available before a significant part of the material is affected is reasonable for all fractions, in agreement with aging studies on micromechanically cleaved $RuCl_3$[20]. Because the reaction is slow yet has an activation energy below room temperature, the molecular kinetics are likely complex, and the analysis should be seen as an approximation.

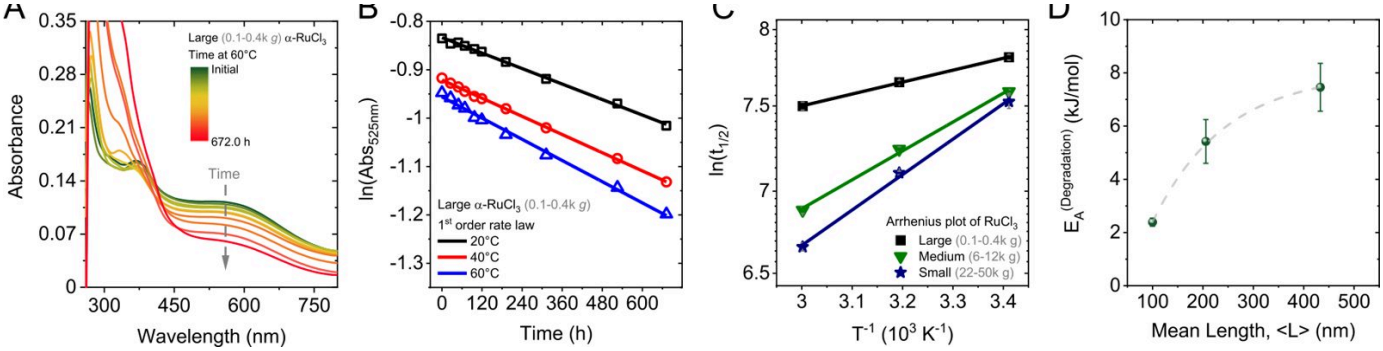

Fig. 6: Spectral changes of large nanosheets at 60 °C over time (A), first-order decay of the absorbance at 525 nm (B), Arrhenius plot of the half-lives (C) and activation energy versus sheet length (D).

The study demonstrates additive-free liquid exfoliation of α-$RuCl_3$ into nanosheets of different sizes and thicknesses in an inert atmosphere, separated into fractions by established cascade centrifugation. TEM confirmed the structural integrity and crystallinity of individual sheets, and Raman spectroscopy, XPS and XRD, averaging over many sheets, supported the picture while exposing the material's tendency to oxidize. For the first time, susceptibility was measured on α-$RuCl_3$ nanosheets in a liquid medium and compared with randomly restacked sheets in drop-cast films. No QSL state could be confirmed for any sheet size; instead, high-temperature antiferromagnetic correlations are suppressed on downsizing while a sharp, 3D-like antiferromagnetic transition appears to be stabilized. The optical response yielded metrics for the average layer number and the concentration in dispersion, with an unusually small change of the extinction and absorbance intensity ratio with lateral size that, although qualitatively similar to other material systems[21],[45],[46], is too small to serve as a reliable metric.

"We consider the presented results important for future applications exploiting magnetic properties of nanosheets," the authors conclude. "The low activation energy for the material decomposition emphasises that the exfoliation, storage and processing parameters can lead to significant differences in material characteristics attributed to partial oxidation of the nanomaterial and have to be studied carefully before applications can be considered."

What the work changes is the starting point: pristine, undoped α-$RuCl_3$ nanosheets of controlled size can now be made in quantity and in liquid, and their magnetism can be studied as a function of size rather than only in bulk crystals or single mechanically cleaved flakes. The atomic-scale proof that the sheets kept their trigonal lattice, and the first direct comparison of experimental HRTEM images with simulations of the known polymorphs, came from aberration-corrected low-voltage TEM at 80 kV at Ulm University, which also set the limit: below about six layers the beam alters the lattice faster than it can be imaged. Finding out how the magnetism of such ultrathin sheets develops, and whether the stabilized antiferromagnetic phase or a spin liquid wins at the monolayer limit, is the next step.

Resource

Synnatschke, K., Jonak, M., Storm, A., Laha, S., Köster, J., Petry, J., Ott, S., Szydłowska, B., Duesberg, G. S., Kaiser, U., Klingeler, R., Lotsch, B., Backes, C. (2023). Sonication-assisted liquid exfoliation and size-dependent properties of magnetic two-dimensional α-$RuCl_3$.

J. Phys. D: Appl. Phys. **56**(27), 274001.
https://doi.org/10.1088/1361-6463/accc3e

References

1. Balents, L. (2010). Spin liquids in frustrated magnets. *Nature*, **464**, 199–208. https://doi.org/10.1038/nature08917
2. Banerjee, A., Bridges, C. A., Yan, J.-Q., Aczel, A. A., Li, L., Stone, M. B., Granroth, G. E., Lumsden, M. D., Yiu, Y., Knolle, J., Bhattacharjee, S., Kovrizhin, D. L., Moessner, R., Tennant, D. A., Mandrus, D. G., & Nagler, S. E. (2016). Proximate Kitaev quantum spin liquid behaviour in a honeycomb magnet. *Nature Materials*, **15**, 733–740. https://doi.org/10.1038/nmat4604
3. Knolle J, Kovrizhin D L, Chalker J T and Moessner R 2014. Dynamics of a two-dimensional quantum spin liquid: signatures of emergent Majorana fermions and fluxes. Phys. Rev. Lett. 112 207203. https://doi.org/10.1103/physrevlett.112.207203 https://doi.org/10.1103/physrevlett.112.207203
4. Nayak C, Simon S H, Stern A, Freedman M and Das Sarma S 2008 Non-Abelian anyons and topological quantum computation. Rev. Mod. Phys. 80 1083–159 https://doi.org/10.1103/revmodphys.80.1083 https://doi.org/10.1103/revmodphys.80.1083
5. Cao H B, Banerjee A, Yan J Q, Bridges C A, Lumsden M D, Mandrus D G, Tennant D A, Chakoumakos B C and Nagler S E 2016 Low-temperature crystal and magnetic structure of α-$RuCl_3$. Phys. Rev. B 93 134423 https://doi.org/10.1103/physrevb.93.134423 https://doi.org/10.1103/physrevb.93.134423
6. Kubota Y, Tanaka H, Ono T, Narumi Y and Kindo K 2015 Successive magnetic phase transitions in α-$RuCl_3$: XY-like frustrated magnet on the honeycomb lattice. Phys. Rev. B 91 094422. https://doi.org/10.1103/physrevb.91.094422 https://doi.org/10.1103/physrevb.91.094422
7. Sears, J. A., Songvilay, M., Plumb, K. W., Clancy, J. P., Qiu, Y., Zhao, Y., Parshall, D., & Kim, Y.-J. (2015). Magnetic order in α-$RuCl_3$: A honeycomb-lattice quantum magnet with strong spin-orbit coupling. *Physical Review B*, **91**, 144420. https://doi.org/10.1103/physrevb.91.144420
8. Majumder M, Schmidt M, Rosner H, Tsirlin A A, Yasuoka H and Baenitz M 2015 Anisotropic Ru^{3+} $4d^5$ magnetism in the α-$RuCl_3$ honeycomb system: susceptibility, specific heat, and zero-field NMR.Phys. Rev. B 91 180401. https://doi.org/10.1103/physrevb.91.180401 https://doi.org/10.1103/physrevb.91.180401
9. Weber D, Schoop L M, Duppel V, Lippmann J M, Nuss J and Lotsch B V 2016 Magnetic properties of restacked 2D spin 1/2 honeycomb $RuCl_3$ nanosheets.Nano Lett. 16 3578–84. https://doi.org/10.1021/acs.nanolett.6b00701 https://doi.org/10.1021/acs.nanolett.6b00701
10. Wang L, Rocci-Lane M, Brazis P, Kannewurf C R, Kim Y-I, Lee W, Choy J-H and Kanatzidis M G 2000 α-$RuCl_3$ /polymer nanocomposites: the first group of intercalative nanocomposites with transition metal halides. J. Am. Chem. Soc. 122 6629–40. https://doi.org/10.1021/ja9944610 https://doi.org/10.1021/ja9944610
11. Fletcher J. M., Gardner W. E., Fox A. C. and Topping G. 1967 X-ray, infrared and magnetic studies of α- and β-ruthenium trichloride. J. Chem. Soc. A 1038–45. https://doi.org/10.1039/j19670001038 https://doi.org/10.1039/j19670001038
12. Kobayashi Y, Okada T, Asai K, Katada M, Sano H and Ambe F 1992 Moessbauer spectroscopy and magnetization studies of α- and β-$RuCl_3$. Inorg. Chem. 31 4570–4. https://doi.org/10.1021/ic00048a025 https://doi.org/10.1021/ic00048a025
13. Lam D, Lebedev D, Kuo L, Sangwan V K, Szydlowska B M, Ferraresi F, Soell A, Sofer Z and Hersam M C 2022 Liquid-phase exfoliation of magnetically and optoelectronically active ruthenium trichloride nanosheets. ACS Nano 16 11315–24. https://doi.org/10.1021/acsnano.2c04888 https://doi.org/10.1021/acsnano.2c04888
14. Pecha R and Gompf B 2000 Microimplosions: cavitation collapse and shock wave emission on a nanosecond time scale. Phys. Rev. Lett. 84 1328–30. https://doi.org/10.1103/physrevlett.84.1328 https://doi.org/10.1103/physrevlett.84.1328
15. Hernandez Y, Lotya M, Rickard D, Bergin S D and Coleman J N 2010 Measurement of multicomponent solubility parameters for graphene facilitates solvent discovery. Langmuir 26 3208–13. https://doi.org/10.1021/la903188a https://doi.org/10.1021/la903188a
16. von Schnering, H. G., Brodersen, K., Moers, F., Breitbach, H. K., & Thiele, G. (1966). Strukturuntersuchungen an β-$RuCl_3$, $RuBr_3$ und RuJ_3. *Journal of the Less Common Metals*, **11**, 288–289. https://doi.org/10.1016/0022-5088(66)90016-6
17. Linck M, Hartel P, Uhlemann S, Kahl F, Mueller H, Zach J, Haider M, Niestadt M, Bischoff M, Biskupek J, Lee Z, Lehnert T, Börrnert F, Rose H, and Kaiser U 2016 Chromatic aberration correction for atomic resolution TEM imaging from 20 to 80 kV. Phys. Rev. Lett. 117 076101. https://doi.org/10.1103/physrevlett.117.076101 https://doi.org/10.1103/physrevlett.117.076101
18. Malis, T., Cheng, S. C., & Egerton, R. F. (1988). EELS log-ratio technique for specimen-thickness measurement in the TEM. *Journal of Electron Microscopy Technique*, **8**, 193–200. https://doi.org/10.1002/jemt.1060080206
19. Backes C, Hanlon D, Szydlowska B M, Harvey A, Smith R J, Higgins T M and Coleman J N 2016 Preparation of liquid-exfoliated transition metal dichalcogenide nanosheets with controlled size and thickness. J Vis. Exp. 118 e54806. https://doi.org/10.3791/54806 https://doi.org/10.3791/54806
20. Du, L., Huang, Y., Wang, Y., Wang, Q., Yang, R., Tang, J., Liao, M., Shi, D., Shi, Y., Zhou, X., Zhang, Q., & Zhang, G. (2019). 2D proximate quantum spin liquid state in atomic-thin α-$RuCl_3$. *2D Materials*, **6**, 015014. https://doi.org/10.1088/2053-1583/aaee29
21. Synnatschke K, Shao S, van Dinter J, Hofstetter Y J, Kelly D J, Grieger S, Haigh S J, Vaynzof Y, Bensch W and Backes C 2019 Liquid exfoliation of $Ni_2P_2S_6$: structural characterization, size-dependent properties and degradation. Chem. Mater. 31 9127–39. https://doi.org/10.1021/acs.chemmater.9b03468 https://doi.org/10.1021/acs.chemmater.9b03468
22. Synnatschke K, van Dinter, J, Mueller, A, Tiede, D, Spillecke, L, Shao, S, Kelly, D, Konecny, J, Konkena, B, McCrystall, M, Saigal, N, Wurstbauer, U, Bensch, W, Sofer, Z, Coleman, J N, Klingeler, R, Haigh, S J and Backes, C 2023 Exfoliability, magnetism, energy storage, and stability of metal thiophosphate nanosheets in liquid medium. 2D Mater. 10 024003. https://doi.org/10.1088/2053–1583/acba2c https://doi.org/10.1088/2053-1583/acba2c
23. Brent J. R., Lewis D. J., Lorenz T., Lewis E. A., Savjani N., Haigh S. J., Seifert G., Derby B. and O'Brien P. 2015 Tin(II) sulfide (SnS) nanosheets by liquid-phase exfoliation of herzenbergite: IV-VI main group two-dimensional atomic crystals. J. Am. Chem. Soc. 137 12689–96. https://doi.org/10.1021/jacs.5b08236 https://doi.org/10.1021/jacs.5b08236
24. Gu J, Du Z, Zhang C, Ma J, Li B and Yang S 2017 Liquid-phase exfoliated metallic antimony nanosheets toward high volumetric sodium storage. Adv. Energy Mater. 7 1700447. https://doi.org/10.1002/aenm.201700447 https://doi.org/10.1002/aenm.201700447
25. Stöter, M., Rosenfeldt, S., & Breu, J. (2015). Tunable exfoliation of synthetic clays. *Annual Review of Materials Research*, **45**, 129–151. https://doi.org/10.1146/annurev-matsci-070214-020830
26. Hanlon D et al 2014 Production of molybdenum trioxide nanosheets by liquid exfoliation and their application in high-performance supercapacitors. Chem. Mater. 26 1751–63. https://doi.org/10.1021/cm500271u https://doi.org/10.1021/cm500271u
27. Harvey, A., He, X., Godwin, I. J., Backes, C., McAteer, D., Berner, N. C., McEvoy, N., Ferguson, A., Shmeliov, A., Lyons, M. E. G., Nicolosi, V., Duesberg, G. S., Donegan, J. F., & Coleman, J. N. (2016). Production of $Ni(OH)_2$ nanosheets by liquid phase exfoliation: from optical properties to electrochemical applications. *Journal of Materials Chemistry A*, **4**, 11046–11059. https://doi.org/10.1039/c6ta02811j

28. Molina-Mendoza A J, Giovanelli, E, Paz, W S, Nino, M A, Island, J O, Evangeli, C, Aballe, L, Foerster, M, van der Zant, H S J, Rubio-Bollinger, G, Agrait, N, Palacios, J J, Perez, E M, and Castellanos-Gomez, A 2017 Franckeite: a naturally occurring van der Waals heterostructure. Nat. Commun. 8 14409. https://doi.org/10.1038/ncomms14409 https://doi.org/10.1038/ncomms14409

29. Lange, R. Z., Synnatschke, K., Qi, H., Huber, N., Hofer, G., Liang, B., Huck, C., Pucci, A., Kaiser, U., Backes, C. and Schlüter, D. 2020 Enriching and quantifying porous single layer 2D polymers by exfoliation of chemically modified van der Waals crystals. Angew. Chem. Int. Ed. 59 5683–95. https://doi.org/10.1002/anie.201912705 https://doi.org/10.1002/anie.201912705

30. Gosch J, Synnatschke K, Stock N and Backes C 2023 Comparative study of sonication-assisted liquid-phase exfoliation of six layered coordination polymers. Chem Commun. 59 55–58. https://doi.org/10.1039/d2cc03366f https://doi.org/10.1039/d2cc03366f

31. Backes, C., Szydlowska, B. M., Harvey, A., Yuan, S., Vega-Mayoral, V., Davies, B. R., Zhao, P. L., Hanlon, D., Santos, E. J., Katsnelson, M. I., Blau, W. J., Gadermaier, C. and Coleman, J. N. 2016 Production of highly monolayer enriched dispersions of liquid-exfoliated nanosheets by liquid cascade centrifugation. ACS Nano 10 1589–601. https://doi.org/10.1021/acsnano.5b07228 https://doi.org/10.1021/acsnano.5b07228

32. Backes C, Higgins T M, Kelly A, Boland C, Harvey A, Hanlon D and Coleman J N 2017 Guidelines for exfoliation, characterization and processing of layered materials produced by liquid exfoliation. Chem. Mater. 29 243–55. https://doi.org/10.1021/acs.chemmater.6b03335 https://doi.org/10.1021/acs.chemmater.6b03335

33. Backes C, Smith R J, McEvoy N, Berner N C, McCloskey D, Nerl H C, O'Neill A, King P J, Higgins T, Hanlon D, Scheuschner N, Maultzsch J, Houben L, Duesberg G S, Donegan J F, Nicolosi V, and Coleman J N 2014 Edge and confinement effects allow in situ measurement of size and thickness of liquid-exfoliated nanosheets. Nat. Commun. 5 4576. https://doi.org/10.1038/ncomms5576 https://doi.org/10.1038/ncomms5576

34. Ridings C, Warr G G and Andersson G G 2012 Composition of the outermost layer and concentration depth profiles of ammonium nitrate ionic liquid surfaces. Phys. Chem. Phys. 14 16088–95. https://doi.org/10.1039/c2cp43035e https://doi.org/10.1039/c2cp43035e

35. Nemes-Incze P, Osváth Z, Kamarás K and Biró L P 2008 Anomalies in thickness measurements of graphene and few-layer graphite crystals by atomic force microscopy in tapping mode. Carbon 46 1435–42. https://doi.org/10.1016/j.carbon.2008.06.022 https://doi.org/10.1016/j.carbon.2008.06.022

36. Gibaja, C., Assebban, M., Torres, I., Fickert, M., Sanchis-Gual, R., Brotons, I., Paz, W. S., Palacios, J. J., Michel, E. G., Abellán, G., & Zamora, F. (2019). Liquid phase exfoliation of antimonene: systematic optimization, characterization and electrocatalytic properties. *Journal of Materials Chemistry A*, **7**, 22475–22486. https://doi.org/10.1039/c9ta06072c

37. Johnson, R. D., Williams, S. C., Haghighirad, A. A., Singleton, J., Zapf, V., Manuel, P., Mazin, I. I., Li, Y., Jeschke, H. O., Valentí, R., & Coldea, R. (2015). Monoclinic crystal structure of α-$RuCl_3$ and the zigzag antiferromagnetic ground state. *Physical Review B*, **92**, 235119. https://doi.org/10.1103/physrevb.92.235119

38. Backes C, Campi D, Szydlowska B M, Synnatschke K, Ojala E, Rashvand F, Harvey A, Griffin A, Sofer Z, Marzari N, Coleman J N, and O'Regan D D 2019 Equipartition of energy defines the size-thickness relationship in liquid-exfoliated nanosheets. ACS Nano 13: 7050–61. https://doi.org/10.1021/acsnano.9b02234 https://doi.org/10.1021/acsnano.9b02234

39. Ziatdinov M, Banerjee A, Maksov A, Berlijn T, Zhou W, Cao H B, Yan J-Q, Bridges C A, Mandrus D G, Nagler S E, Baddorf A P, and Kalinin S V 2016 Atomic-scale observation of structural and electronic orders in the layered compound α-$RuCl_3$. Nat. Commun. 7 13774. https://doi.org/10.1038/ncomms13774 https://doi.org/10.1038/ncomms13774

40. Madsen, J., & Susi, T. (2021). The abTEM code: transmission electron microscopy from first principles. *Open Research Europe*, **1**, 24. https://doi.org/10.12688/openreseurope.13015.2

41. Kraus W and Nolze G 1996 Powder cell-a program for visualization and manipulation of crystal structures and calculation of the resulting X-ray powder patterns. J. Appl. Crystallogr. 29 301–3. https://doi.org/10.1107/s0021889895014920 https://doi.org/10.1107/s0021889895014920

42. Wulferding D, Choi Y, Do S-H, Lee C H, Lemmens P, Faugeras C, Gallais Y and Choi K-Y 2020 Magnon bound states versus anyonic Majorana excitations in the Kitaev honeycomb magnet α-$RuCl_3$. Nat. Commun. 11 1603. https://doi.org/10.1038/s41467–020–15370–1 https://doi.org/10.1038/s41467-020-15370-1

43. Plumb K. W., Clancy J. P., Sandilands L. J., Shankar V. V., Hu Y. F., Burch K. S., Kee H. Y., and Kim Y. J. 2014 α-$RuCl_3$: a spin-orbit assisted Mott insulator in a honeycomb lattice. Phys. Rev. B 90 041112. https://doi.org/10.1103/physrevb.90.041112 https://doi.org/10.1103/physrevb.90.041112

44. Zhou B, Wang Y, Osterhoudt G B, Lampen-Kelley P, Mandrus D, He R, Burch K S and Henriksen E A 2019 Possible structural transformation and enhanced magnetic fluctuations in exfoliated α-$RuCl_3$. J Phys Chem Solids 128 291–5. https://doi.org/10.1016/j.jpcs.2018.01.026 https://doi.org/10.1016/j.jpcs.2018.01.026

45. Backes C, Paton K R, Hanlon D, Yuan S, Katsnelson M I, Houston J, Smith R J, McCloskey D, Donegan J F and Coleman J N 2016 Spectroscopic metrics allow in situ measurement of mean size and thickness of liquid-exfoliated few-layer graphene nanosheets. Nanoscale 8 4311–23. https://doi.org/10.1039/c5nr08047a https://doi.org/10.1039/c5nr08047a

46. Szydlowska B M, Hartwig O, Tywoniuk B, Hartman T, Stimpel-Lindner T, Sofer Z, McEvoy N, Duesberg G S and Backes C 2020 Spectroscopic thickness and quality metrics for $PtSe_2$ layers produced by top-down and bottom-up techniques. 2D Mater. 7 045027. https://doi.org/10.1088/2053–1583/aba9a0 https://doi.org/10.1088/2053-1583/aba9a0